NURETH14-615

EXPERIMENTAL DROPLET DEPOSITION DISTRIBUTION DOWNSTREAM OF FUNCTIONAL SPACERS IN AN ADIABATIC BWR MOCK-UP MODEL

M. Damsohn¹ and H.-M. Prasser¹

ETH Zurich, Switzerland
damsohn@lke.mavt.ethz.ch, prasser@lke.mavt.ethz.ch

Abstract

Functional spacers play an important role for the annular steam-water flow in boiling water reactors. They are designed to enhance droplet deposition and therefore delay dryout by sustaining the liquid film.

To measure droplet deposition distributions downstream of functional spacers, experiments have been conducted in an adiabatic BWR mock-up model of a double subchannel. The experiments were conducted with six different spacer types and three different gas densities. They are designed to produce high-resolved experimental data, both in time in space, by measuring the conductivity distribution in the liquid film, which increases when salt-labeled droplets deposit. The results show, that all studied spacer types enhance the droplet deposition compared to the experiments without spacer. The droplet deposition distribution is very distinct for each spacer shape. The spacer shape, especially the blockage ratio, plays an important role in regard to deposition enhancement. The blockage ratio alone is however not enough to predict deposition. The droplet size distribution seems to shift towards smaller droplets when passing through the spacer. The experiments are also modeled with a Lagrangian-Euler CFD model, which contains turbulence effects on the droplets by means of a random walk model. The model is for some cases in excellent, for other cases in decent agreement with the experiments. The model shows, that the direct droplet-spacer impact and the deflection of streamlines are mainly responsible for the droplet deposition enhancement. For the chosen flow conditions the turbulence plays a minor role for droplet deposition. This might change for BWR conditions.

Introduction

In the upper part of boiling water reactors the flow regime is dominated by a steam-water droplet flow with liquid films on the nuclear fuel rod, the so called (wispy) annular flow regime. The film thickness and liquid flow rate distribution around the fuel rod play an important role especially in regard to dryout, which is the main phenomenon limiting the thermal power of a fuel assembly in boiling water reactors. Functional spacers with different vane shapes have been used in the last decades to enhance droplet deposition and thus create more favorable conditions for the heat removal. The mechanisms for droplet enhancement by functional spacers are discussed widely in literature: Droplet deposition can be accounted to the direct impact of droplets on the spacer creating a lateral momentum needed for deposition on the fuel rod, the deflection of the droplet trajectory due to a change of the gas flow field and turbulence enhancement downstream of the spacer. Droplet deposition has been studied experimentally by integral methods measuring the increase of the mass flux or the increase of conductivity in the liquid film, which increases by droplet deposition with droplets labeled with a salt tracer.

This work aims on experimentally measuring a highly spatially resolved droplet distribution pattern downstream of functional spacers. The measurement is based on measuring the conductance of the liquid film, which increases with salt-labeled droplets depositing in the liquid film. The sensor to measure the conductance is usually used to measure highly dynamic liquid film thickness distributions in annular flow and has been presented by the authors in previous papers [1-3]. Additional CFD calculations complete the picture about the important deposition mechanisms.

1. Experiments

1.1 Experimental Setup

The experiments were conducted in the experimental facility CALVIN (Figure 1). At the heart of this facility is the vertical test section shaped as double subchannel (Figure 2), through which a gas-liquid flow is conducted in upward direction. The gas, shut off from the environment by a water lock, is circulated through the facility by a side channel compressor. Downstream of the test section the water is removed from the gas in the water separator and drained by a pump. A heat exchanger upstream of the test section keeps the temperature of both fluids constant at 20°C.

The test section is manufactured of acrylic glass and has a total length of 2.5 meters. All elevations in this paragraph are given relative to the height of the gas inlet (0 mm): Within the first 500 mm downstream of the gas inlet the channel has a square cross-section of 50 x 50 mm. From 500 mm to 2500 mm the test section has the cross-sectional double subchannel geometry. The sensitive area of the sensor measuring the droplet deposition (described in the next paragraph) is around one of the half cylinders of the double subchannel between the elevation of 2200 mm to 2326 mm. At the height of 500 mm the water injection port of the liquid film is located, the joint between the two different cross-section shapes. The water for the liquid film is demineralized from the lab supply and injected directly unto the wall by a narrow slit of 0.5 mm stretching along the entire circumference of the double subchannel profile.

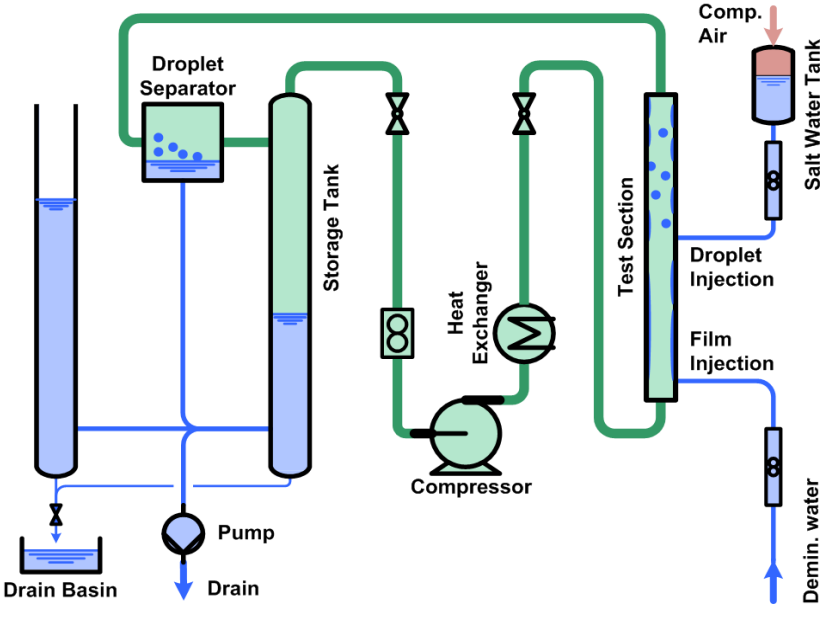


Figure 1 Experimental Setup CALVIN

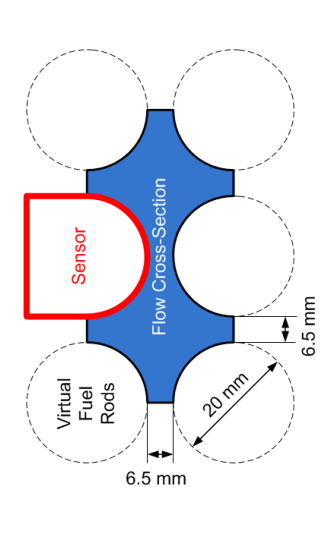


Figure 2 Test section

The droplets, labeled with a salt tracer, are injected at an elevation of 2160 mm (capillary tips) by a special injector (Figure 3). The injector consists of structure with a wall width of 2 mm. Within internal channels inside of the injector the wall, the water is distributed towards 24 capillaries with an inner diameter of 250 µm and an outer diameter of 330 µm. The water is fed into the injector structure by a port at the injector side, where it is touching the test section wall. The labeled water for the droplets is stored in a small pressure vessel and pressed into the injector by an air cushion of roughly 4 bar. Three different spacer shapes (Sp 1, Sp 2 and Sp 3) were tested in the experiments (Figure 4). Sp1 is a generic spacer while Sp2 and Sp3 are similar to spacers used in industrial applications [4, 5]. All of the spacers used are so-called swirl type spacer creating a secondary flow in the subchannel. For each spacer shape two different vane angles are used (A/B-series). Each spacer is mounted in the test section such, that the lower edge of the spacer body is 30 mm upstream of the sensor's sensitive area (Figure 5). With these spacer positions the droplet deposition can be observed directly downstream of the spacer.

In the representation of the results shown in the following chapters, the lowest line of the sensor sensitive area is referred to as 0 mm.

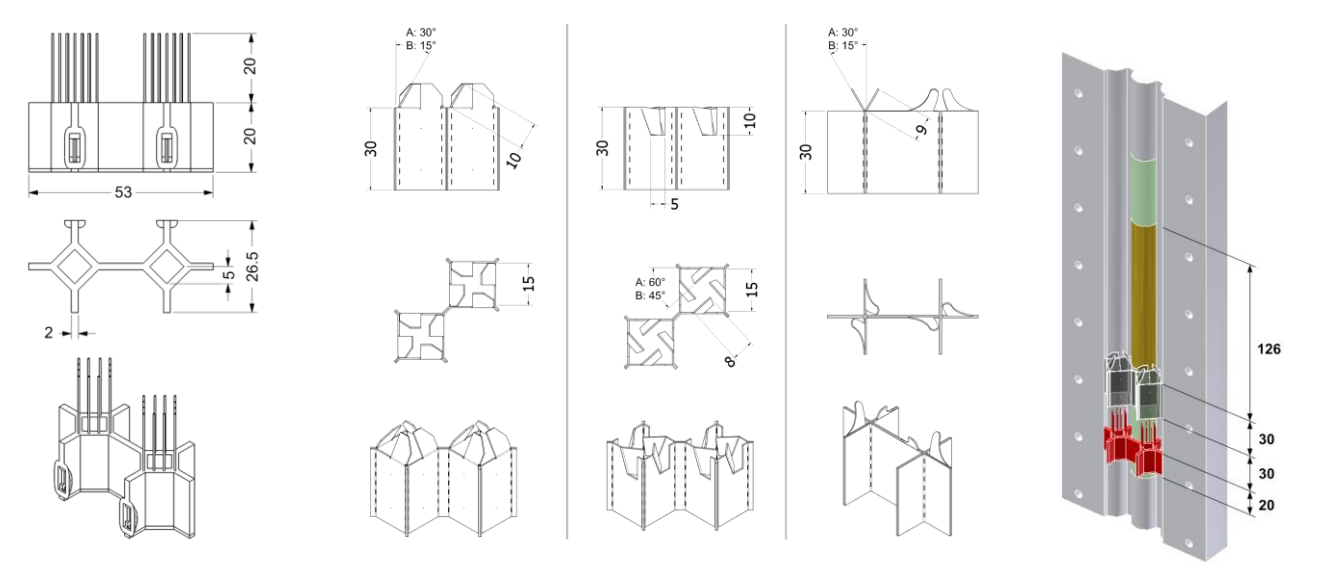


Figure 3 Droplet injector

Figure 4 Spacer geometries: Spacer 1 (left), Spacer 2 (center), Spacer 3 (right)

Figure 5 Spacer and drop injector position

1.2 Liquid Film Sensor

The basic idea for the fast acquisition of time sequences of two-dimensional droplet deposition distributions is an array of electrode pairs mounted flush to the wall. When a voltage pulse is supplied to the first electrode (transmitter electrode) of each pair, a current flows to the second electrode (receiver electrode), that is kept at zero potential. The current is depending on the conductance of an electrically conducting liquid film covering both electrodes. This conductance is depending on the conductivity of the liquid and the film thickness. The methodology to extract droplet deposition parameters from the conductance will be described in the next paragraph. The electrode pairs are arranged around a half cylinder with 20 mm diameter in a 64x16 matrix with a periodic pitch of 2 x 2 mm² corresponding to 12° pitch around the circumference. The conductance between the electrode pairs is acquired with 10'000 fps and represents the liquid film thickness on the sensor surface. The sensor is also used to measure film thickness distributions. Details can be found in [1-3].

1.3 Experimental Conditions

All experiments were conducted at a temperature of $20^{\circ}C$ and a static pressure of about 1.1 bar at the sensor location, the pressure depending slightly on the velocities of the media. These conditions are very different from the conditions in a BWR. The experiments are designed for CFD validation in a BWR similar flow geometry. The injected water for the liquid film was demineralized water with a conductivity of $0.7~\mu S/m$. The conductivity of the injected droplets was between 6300 and 34800 $\mu S/m$. The conductivity was adjusted by mixing NaCl such that the primary signal on the sensor was never above the measuring limit of the data acquisition unit.

G	as	Helium					Air					C ₄ F ₈				
	1-p [-]	0.0100	0.0080	090000	0.0040	0.0020	0.0100	0.0080	090000	0.0040	0.0020	0.0100	0.0080	090000	0.0040	0.0020
	10											X	Х	Χ	X	Х
_	15															
<u>[</u> S]	20						X	X	X	X	X	X	X	X	X	X
Έ	25	X	X	X	X	X	X	X	X	X	X	X	X	X	X	X
J [m/s]	30	X	X	X	X	X	X	X	X	X	X	X	X	X	X	X
_	35															
	40		X	X	X	X										
• •						1-10										

Table 1 Experimental matrix for the droplet deposition experiments

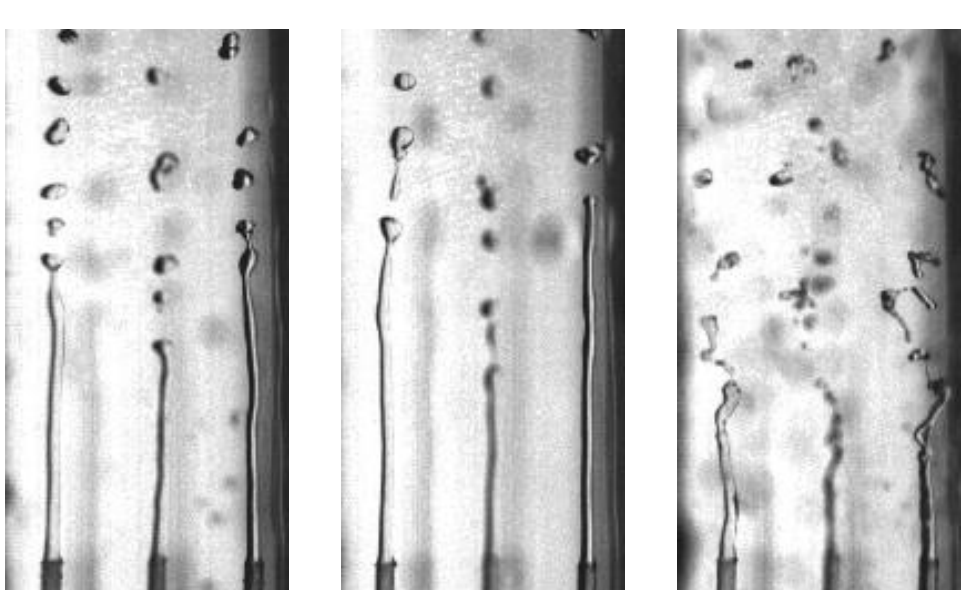


Figure 6 HSC images of droplet injection for helium (left), air (center) and C_4F_8 (right) for a gas velocity of 30 m/s

The gas circulated in the setup was either helium, air or C_4F_8 . Furthermore, the experiments were conducted without spacer and with the six different spacer shapes in place. Table 1 shows the matrix of conducted experiments based on the variation of the flux ratio 1- β and the total flux J. Certain constraints are limiting the full variation of these parameters, either the limits of the experimental setup

or the departure from annular flow conditions. The droplet flow rate is 10 l/h for all experiments, resulting in an injection velocity of 2.3 m/s.

The generated droplet size distribution and the width of the drop injection cone were taken from high-speed camera (HSC) images taken in preliminary experiments without liquid film on the test section walls. Because the drop size distribution and the injection cone angle are functions of the gas velocity and gas density, these parameters were determined under variation of these flow conditions corresponding to the test matrix in Table 1. Figure 6 shows a snapshot of the HSC images just downstream of the capillary tips for three different gases. The influence of the liquid film on the model rod in regard to drop formation at the capillary tip is assumed to be negligible.

With this injection Stokes numbers are always in the range between 1000 and 2000, which means that the trajectories of the droplets are very much inertia controlled. The initial droplet velocity is assumed to be the injected volume flow rate divided by the sum of all capillary cross-sections.

For all experiments, conductance distributions were measured with a rate of 10000 frames per second over a period of 10 seconds. This has shown to give sufficient statistics.

1.4 Post-processing Methods

There are two different methods for characterizing the droplet deposition by post-processing of the measuring data, when the droplets are marked with a higher conductivity:

- Estimating the total mass transfer of droplets onto the liquid film by determining the timeaveraged conductance increase compared to a flow without droplet deposition.
- Counting single droplet impacts by filtering with an autoregressive model trained to the interfacial wave structures

The combination of both methods gives best possible insights into the physical background of droplet deposition.

1.4.1 <u>Droplet Deposition Estimation by Time-Averaged Signal Analysis</u>

The total mass transfer caused by droplet deposition is best estimated by evaluating the time-averaged conductance signal of the liquid film sensor. The conductance at each measuring point is a function of the film thickness and the conductivity of the liquid covering the measuring point. When droplets of higher conductivity are deposited onto the liquid film with lower conductivity, then the conductivity in the liquid film rises as a result of mixing. The contribution in the measured signal due to film thickness or increased conductivity can be separated by measuring the time-averaged film thickness in a reference experiment, where the droplets are injected with the same conductivity as the liquid film, usually demineralized water. In this case, the conductance only depends on the film thickness. Knowing the film thickness under reference conditions, the mass transfer rate in the experiment with marked droplets can be calculated on basis of a mass balance for the salt tracer, which is proportional to the corresponding conductivity (Equation 1). In a control volume of the liquid film, mass flow rate m and conductivity c with index d for deposited droplets and index f for the liquid film are connected as follows, if entrainment is neglected:

$$\dot{m}_{f,in} \cdot c_{f,in} + \dot{m}_{d,in} \cdot c_{d,in} - \dot{m}_{f,out} \cdot c_{f,out} = 0 \tag{1}$$

Since the mass flow rate of droplets is small compared to the mass flow rate of the liquid film one can assume that the incoming and outgoing mass flow rate of the liquid film are equal. The error caused by the simplification has been proven to be negligible.

With this assumption, the mass flow rate of deposited droplets is:

$$\dot{m}_{d,in} = \dot{m}_{f,in} \cdot \frac{c_{f,in}}{c_{d,in}} \cdot \left(\frac{c_{f,out}}{c_{f,in}} - 1\right) \tag{2}$$

If the control volume is chosen such that it starts from the most upstream point of the sensor to the point of interest, then $c_{f,in}$ is the conductivity of the liquid injected as film. Variable $c_{d,in}$ is the conductivity of the liquid injected as droplets. Furthermore the dimensionless concentration $\omega = c_{f,out}/c_{f,in}$ describes the quantity of the liquid originating from the droplet deposition at the point of interest. The dimensionless concentration is directly received from the measurements by referring the measuring signal s with labelled droplets to the signal of the reference measurement with unlabelled droplets, as defined by Equation (3).

$$\omega = \frac{c_{f,out}}{c_{f,in}} = \frac{s_{with \ labelled \ droplets}}{s_{with \ unlabelled \ droplets}}$$
(3)

The referencing of the measurement signal compensates the influence of the film thickness on the measuring signal, because the time-averaged film thickness is equal in the measurement with labelled and unlabelled droplets. It should be noted, that it is assumed that there is no time-averaged inhomogeneous conductivity distribution perpendicular to the wall, that causes a non-linear relation between the measured signal and the average conductivity of the control volume. It should further be noted, that droplets originating from the entrainment process of the liquid film, are not considered when quantifying the deposition rate, because they cannot be detected by the sensor. The dimensionless concentration is affected by three different phenomena in annular flow: The place of droplet deposition, the advection of the deposited mass in the liquid film and the turbulent and molecular diffusion in the liquid film. This means, that strictly speaking the locations of droplet deposition can only be deducted from the dimensionless concentration, if the lateral advection and diffusion in the liquid film are known, which is not the case for the conducted experiments. When averaging the dimensionless concentration in circumferential direction on the other hand, the droplet deposition rate can be determined quite exact as function of the axial position, because it is independent of the circumferential advection and diffusion. This is the so called deposition profile. To qualify the performance of a spacer regarding droplet deposition, the fraction of deposited mass downstream of the spacer compared to the total droplet mass upstream of the spacer is a more important quantity than the dimensionless concentration. This so-called integral droplet deposition fraction Θ can be determined by Equation (4).

$$\theta = \frac{\dot{m}_{d,in} \cdot P}{\dot{m}_{d,total} \cdot l_{mp}} \tag{4}$$

Where P is the perimeter of the test section and l_{mp} is the width of a measuring point of the sensor. The injected mass flow rate $m_{d,total}$ is known from the flow meter of the droplet injector, while $m_{d,in}$ is the deposited mass determined by Equation (2).

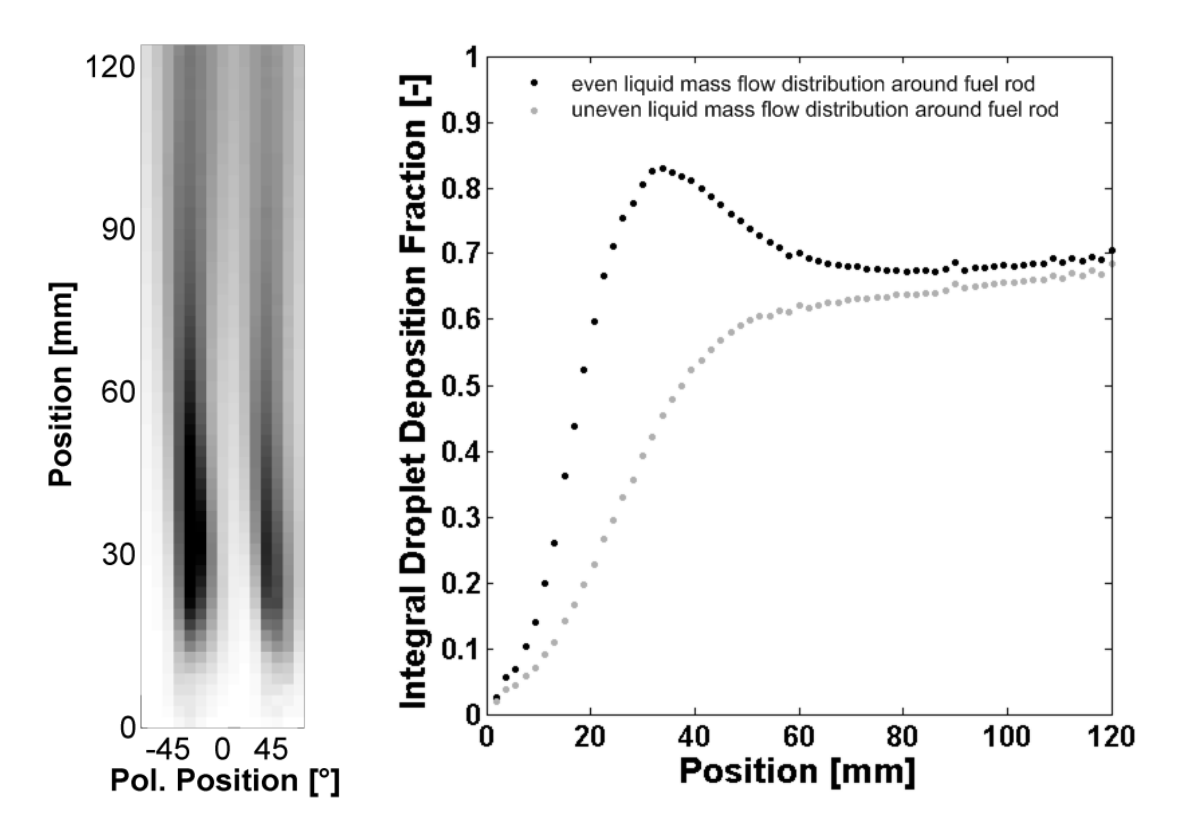


Figure 7 Droplet deposition distribution and profile for Sp1-A (J=25, 1-β=0.01, air)

The integral deposition fraction can take locally a bigger value than unity, if the droplet deposition is not distributed equally around the perimeter. The circumferentially averaged integral droplet deposition however (deposition profile) has to be smaller than one per definition. Figure 7 shows the integral droplet deposition fraction, shown as a spatial distribution and deposition profile. An uncertainty on the integral droplet deposition fraction is introduced, if the film mass flow rate into the control volume $m_{f,in}$ is unknown. Without any obstacles in the flow field, the liquid mass flux can be assumed to be equally distributed around the perimeter, such that $m_{f,in}$ is known. With obstacles mounted in the test section this assumption can be violated: Such a case is seen in Figure 7. The overshoot in the upper curve results from a high droplet deposition rate at a reduced local mass flow rate, namely the spot of thin film thickness just downstream of a spacer mounted in the test section. Further downstream of the spacer, where the mass flux redistributes laterally, this overshoot disappears. The effect cannot be compensated for, because the real spatial mass flow rate distribution is not measured and therefore not available. A conservative approximation is the assumption, that the mass flow rate scales linear with the film thickness (lower line in Figure 7).

All results shown later, are obtained for the more conservative approximation of a non-uniform liquid mass flow rate distribution.

1.4.2 Droplet Deposition Estimation by Autoregressive Filtering in the Time Domain (Count-Based)

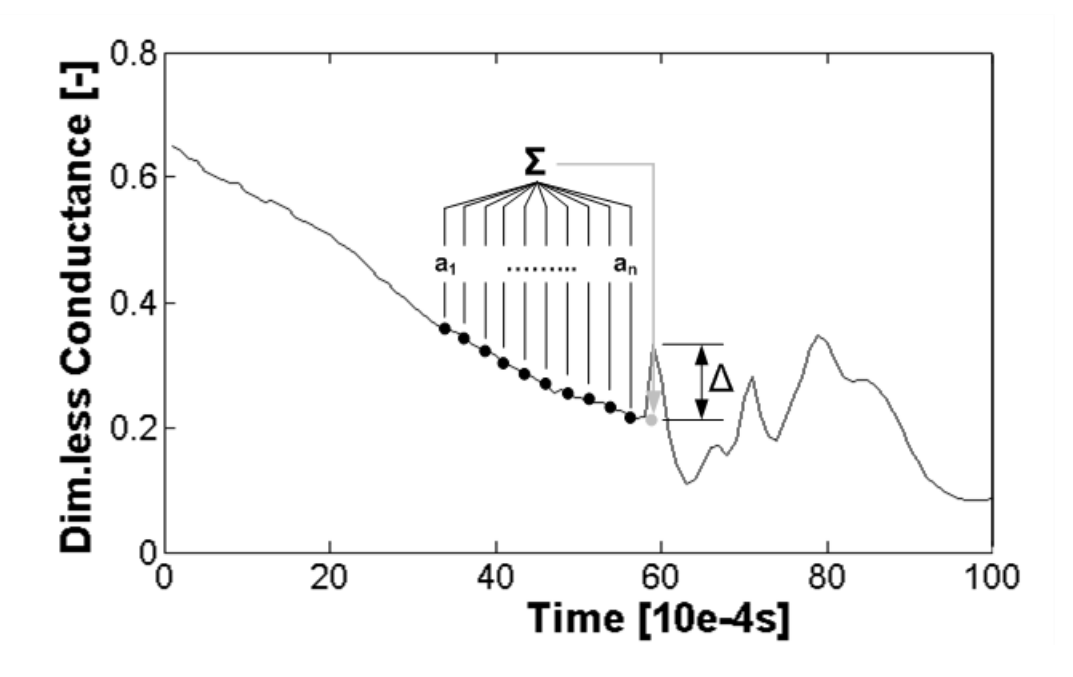


Figure 8: Principal of autoregressive droplet impact filtering

The detection and counting of single droplet impacts faces the challenge to separate droplet impacts from wavy structures of the liquid film. This is especially challenging in the presence of roll waves that already transport liquid of higher conductivity. Rapid changes of the measured conductance signals are the consequence, which are similar to the fingerprint of a droplet impact. The detection of droplet impacts is carried out by the help of an autoregressive model trained to the sensor signal sampled at a single measuring point. The autoregressive filter uses the fact, that droplet impacts are rare events interrupting the signal sequence, which is characteristic for interfacial structures on the liquid film of a certain experiment.

The filter is based on the prediction of the signal at a certain instant in time \tilde{s}_i by the autoregressive model using n earlier points in time s_{k-i} . The residuum between the prediction and the real measured signal is high in the presence of a sudden disturbance like a droplet impact (Figure 8). The signal is predicted by the sum of the n=10 previous signal points weighted by coefficients a_i (Equation 5). These weighting factors a_i are optimized by the total time signal of one measuring point to give a minimum sum of differences in the time domain using the method of least squares according to Equation 6. Because the transient behavior might change depending on the location on the sensor, especially in presence of flow obstacles like spacers, the weighting factors are optimized for each measuring point individually to predict the wave structures present in the flow as accurate as possible. Rare events like a droplet impact generate a high difference between the predicted and measured signal, the so called residuum Δ .

$$\tilde{s}(x,y)_{k} = \sum_{i=1}^{n} a_{i} s(x,y)_{k-i}$$
(5)

$$\psi = \sum_{k=n+1}^{m} \left(\tilde{s}_k - s_k \right)^2 = \min$$
 (6)

The method is very reliable for horizontal flows [6], because the roll waves contain less higher characteristic frequencies in a horizontal channel than the roll waves in a vertical channel. It was found that for the vertical channel, high values of the residuum Δ can be caused by roll waves, which create spurious detections of droplet depositions. To distinguish if a high residuum is generated by roll waves or by droplet deposition, the surrounding measuring points of the sensor are taken into account, because besides the high frequency the spatial extension of the impact is very distinct for a droplet impact. The spatial filtering reduces the spurious detection substantially.

2. Results

2.1 Time-Averaged Droplet Deposition Distribution

Figure 9 shows the integral droplet deposition fraction for the six different spacers and once without spacer for an air-water flow shown as a two-dimensional distribution on the sensor surface. The gray scale represents the integral mass deposition.

For the experiments without spacers, the droplet deposition mainly occurs around the lines of -45° and 45° circumferential position (Figure 9), the so called subchannel sides. All spacers enhance the droplet deposition more in the subchannel side than in the subchannel gap. Because of their symmetric shape, Sp1 and Sp2 produce a periodic pattern in the circumferential direction. Sp3 enhances the deposition at the side, where the spacer vane is close to the surface of the fuel rod model.

Figure 10 to Figure 13 shows deposition profiles, which are the axial integral droplet deposition fraction averaged in circumferential direction. Comparing across different gas densities (Figure 9), it can be seen that the droplet deposition caused by the spacer Sp2-A is almost independent from the gas density. There is a bit less total deposition for the case of C_4F_8 , but the deposition profile is slightly steeper in the beginning. Because the Stokes number of the injected droplets is nearly equal for the three different gases, the deposition driven by a deflection of the droplet trajectory caused by the drag of the gaseous phase, shortly termed drag deflection, cannot be the cause of the difference.

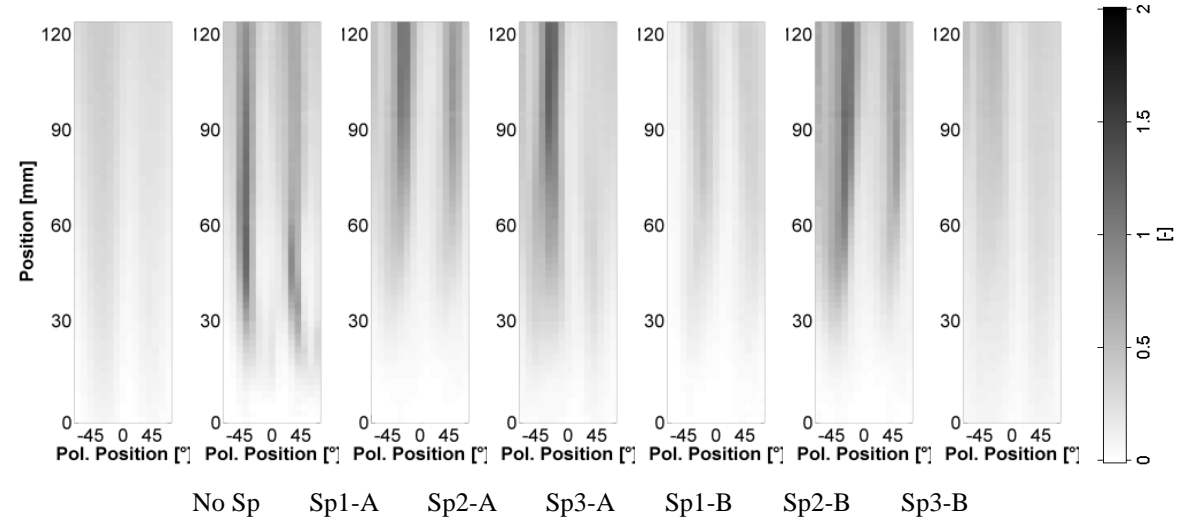


Figure 9 Integral droplet deposition fraction distribution for different gases (air) and spacers (J=30 m/s, $1-\beta=0.002$)

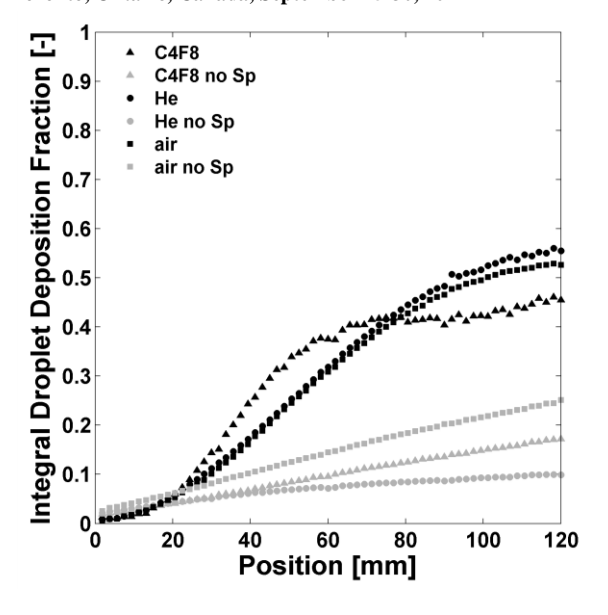
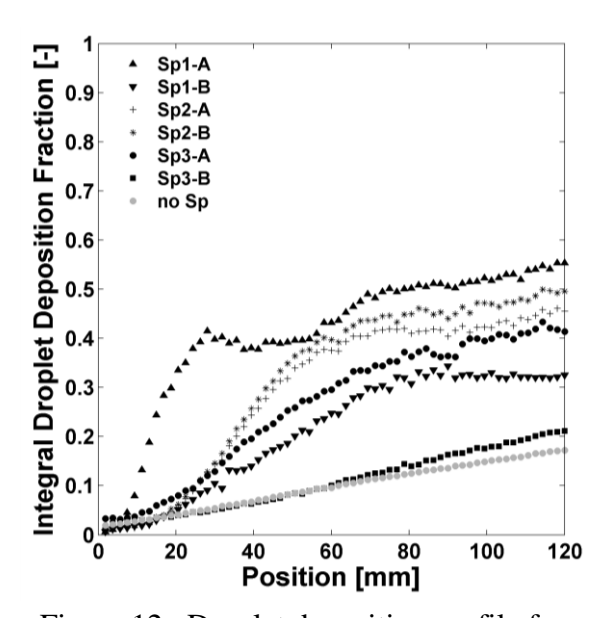


Figure 10 Droplet deposition profile for different gases (Sp2-A and without spacer, $J=30 \text{ m/s}, 1-\beta=0.002$)

Figure 11 Droplet deposition profile for flux ratios (Sp2-A, J=30 m/s, C₄F₈)



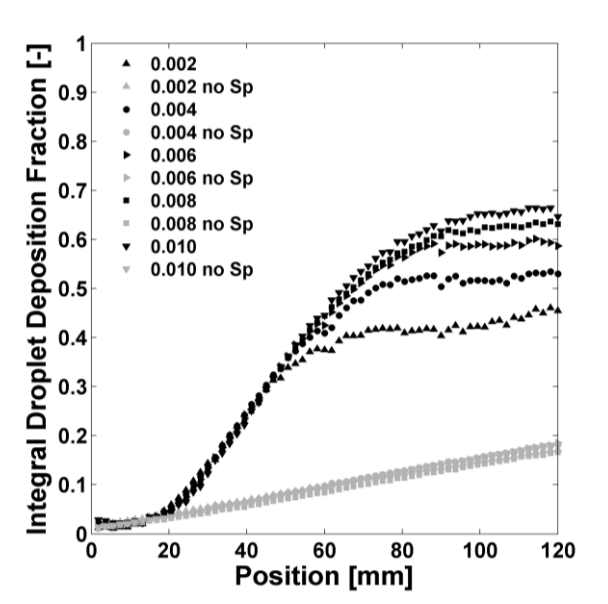


Figure 12 Droplet deposition profile for different spacers (J=30 m/s, 1- β =0.002, C₄F₈)

Figure 13 Droplet deposition profile for total fluxes (Sp2-A, $1-\beta=0.002$, C_4F_8)

This means that reflection of droplets impacting the spacer structures is the most probable explanation. There has to be droplet breakup when droplets impact on the spacer. The emitted secondary droplets causes the first increase of deposition. Because the deposition profiles have similar gradients from 80 mm downstream, the deposition in this area is probably finally caused by drag deflection. The smallest deposition rate is observed in case of C_4F_8 , which underlines the necessity to carefully assess the phenomenological approach for the BWR spacer design.

Figure 12 compares the different spacer deposition profiles for the C_4F_8 -water flow. It is seen across all spacer types, that spacer with a higher blockage ratio cause a better droplet deposition.

The smallest difference is seen for Sp3-B, where a vane angle of 15° barely enhances the droplet deposition compared to the case without spacer.

Sp1-A has a very steep profile in close proximity to the spacer (5 mm to 25 mm downstream), which is most probably caused by the highest blockage ratio. The other spacers have a wider stretched deposition area between 10 to 60...80 mm downstream, before the enhancement of the deposition is vanishing: the gradient of the integral droplet deposition is equal or in some cases less than the very linear behavior in the experiment without spacer.

The simulations later in this work will show, that the first increase is most probably driven by direct impacts of droplets with the spacer, while the less pronounced droplet deposition further downstream is driven by drag deflection.

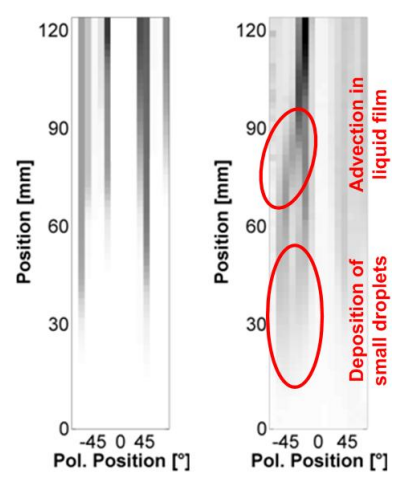
Figure 12 shows the deposition profiles for Sp3-A under the influence of different flux ratios for the C₄F₈-water flow. Without spacer, there is basically no increase of deposition rates with higher flux ratios, even though the mean liquid film thickness increases. The deposition is on the other hand increasingly growing with increasing flux ratio when there are spacers present in the flow. It is interesting to see that for flows with spacers the deposition enhancement is identical for the first 45 mm downstream of the spacer, before coming under the influence of the flux ratio. This can be explained by the two-fold deposition mechanism: Within the first 45 mm the deposition is mainly driven by the direct interaction with the spacer, where the droplets splash of the spacer and the residence time in the channel is strongly below the relaxation time. The impact driven deposition is therefore independent of the flux ratio. Further downstream, the droplets driven by the drag deflection are swallowed earlier by a thicker liquid film, when they get close to the channel wall. Figure 13 shows the influence of the total flux on the droplet deposition for the C₄F₈-water flow without spacer and in presence of Sp3-A. It is interesting that the total flux plays a minor role in the deposition mechanism. This minor dependency on the gas velocity shows, that the major contribution for droplet deposition behind a spacer is not drag deflection but the direct impact of the droplets with the spacer. Concluding it can be said, that the behavior of spacers in regard to droplet deposition is hard to predict with simple parameters, as the dependence on the flux ratio, gas density and spacer shape are strongly nonlinear. From a generic point of view, this makes desirable a CFD based approach in regard to spacer design.

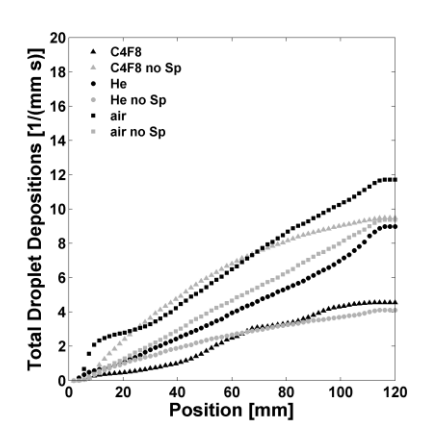
2.2 Count-Based Droplet Deposition

The autoregressive filter allows determining the local droplet deposition intensity, which is difficult or, respectively, very inaccurate by calculating the derivative of the integral time-averaged mass deposition, because it is distorted by non-axial liquid velocity fields. On the other hand, the detection of droplet deposition events can only lead to a rough estimate of the deposited mass, since the droplet size, especially downstream of the spacer, is unknown.

Figure 14 shows the integral droplet deposition count per millimeter circumferential distance and per second. The integral deposition count is the local deposition count integrated along the axial direction. The integral droplet deposition count is in contrast to the integral droplet deposition fraction not directly measured by the sensor. It is still chosen to be displayed rather than the local droplet deposition count, to make it comparable to the integral droplet deposition fraction. The difference between the two is that the integral droplet deposition count is artificially integrated in axial direction, while the integral droplet deposition fraction is integrated by the advective and diffusive transport in the liquid film. Therefore a significant discrepancy is expected especially if spacers are present.

Concerning the circumferential location of droplet deposition, there is only minor differences seen between the two post-processing methods.





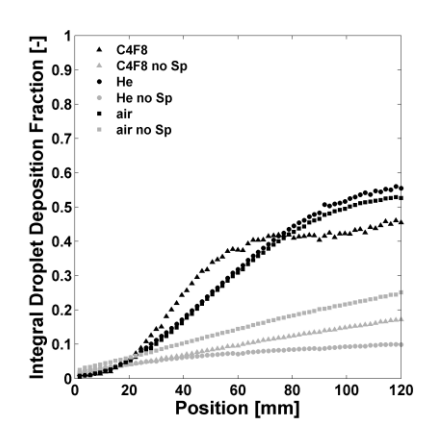


Figure 14 Count-based (left) and time-averaged (right) droplet deposition distrib. (Sp3-A, J=30 m/s, 1-β=0.002, C₄F₈)

Figure 15 Count-based (left) and time-averaged (right) droplet deposition profile for different gases (Sp2-A and without spacer, J=30 m/s, 1-β=0.002)

Figure 14 is a chosen case to compare the integral droplet deposition fraction with the count based method. It should be noted, that the color scale is not quantitatively comparable, because the droplet deposition count and droplet deposition fraction are to different physical quantities. The comparison is therefore of qualitative nature.

Figure 14 also shows a good agreement between the count-based and time-averaged method. The presence of a spacer however causes an advective transport in circumferential direction within the liquid film, which causes the discrepancy in the marked point. Diffusion of liquid originating from droplet deposition in circumferential direction within the liquid film is also visible. The droplet deposition closest to the spacer for the time-averaged method is not seen in the count-based results. An hypothesis is that the droplets depositing in this area are smaller than the detection limit of the autoregressive filter.

From the discrepancy in the results between count-based and time averaged method, it can therefore be concluded that the droplets passing the spacer undergo breakup, which causes small droplets to deposit in spacer proximity. The droplet breakup can either occur by direct impact of droplets with the spacer or by an increased shear in the gas flow in spacer proximity.

The hypothesis of break-up is further supported by a comparison of the count-based and time-averaged droplet deposition profile, as displayed in Figure 15. For the figures it should be pointed out, that the units at the y-axis are different for the two graphs. Therefore only a qualitative comparison is possible. From the results of the time-averaged method in Figure 15 (bottom) it would be expected that there are more droplet deposition counts when there is a spacer present compared to a case without spacer, because it is seen, that the transferred droplet mass is increased. The count-based results however show, that the droplet deposition counts are in the same order of magnitude or even less if a spacer is present compared to deposition counts without spacer. This discrepancy between the transferred mass and droplet count can only be explained with droplet break-up, causing deposition below the detection limit of the autoregressive filter. This deposition increases the transferred mass in the liquid film without droplet impacts being detected.

3. CFD Simulation

The geometry is reflected in the CFD code by an unstructured polyhedral mesh with an approximate cell diameter of 2 mm, the so-called base size (Figure 16). Unlike in the experiment, the subchannel is considered to have a periodic condition in the subchannel gap. With this difference between the experimental and simulation domain, the computational cost is reduced substantially, because only a quarter of the subchannel has to be modeled for Sp1 and Sp2 which are 90° periodic. The mesh size is reduced in spacer proximity and close to the walls.

For simplicity, the k-\varepsilon-turbulence model was chosen. A sensitivity study on the mesh size, turbulence model, wall treatment and the periodic boundary conditions is shown in chapter 4.1.1.

The model for droplet motion is implemented as an one-way-coupled Euler-Lagrangian model in STAR-CCM+. The model is based on the work of Gosman [7]. The first step in the simulation process is the calculation of the steady-state CFD solution of the gas velocity field. In this stage, the solver for the Lagrangian droplet tracking is switched-off. After convergence of the flow field, the Lagrangian solver is turned on. 10'000 droplets per nozzle are launched from the locations of the injection nozzles and tracked in the simulation domain. The droplet properties, namely the drop size distribution and the injection cone angle, are taken from the afore shown HSC images. Droplets are counted as deposited, when the trajectory virtually penetrates the fuel rod wall. They are considered to be absorbed and are not further tracked in the simulation. The same counts for droplets leaving the outlet of the domain. Droplets impacting on the spacer are considered to lose all their momentum perpendicular to the wall. They are not leaving the calculation domain, but are further tracked. The approximation of full momentum loss is chosen, as it is closest to the buildup of a liquid film on the spacer and a shear-off at the spacer edge. This assumption is discussed in the sensitivity study. Droplet break-up and coalescence are not considered in the simulation, because the modeling of these processes insert a high uncertainty that cannot be validated with the experiments of this work.

The simulation is conducted without taking into consideration the liquid film, neither by the reduction of the cross-section nor in the sense of wall roughness.

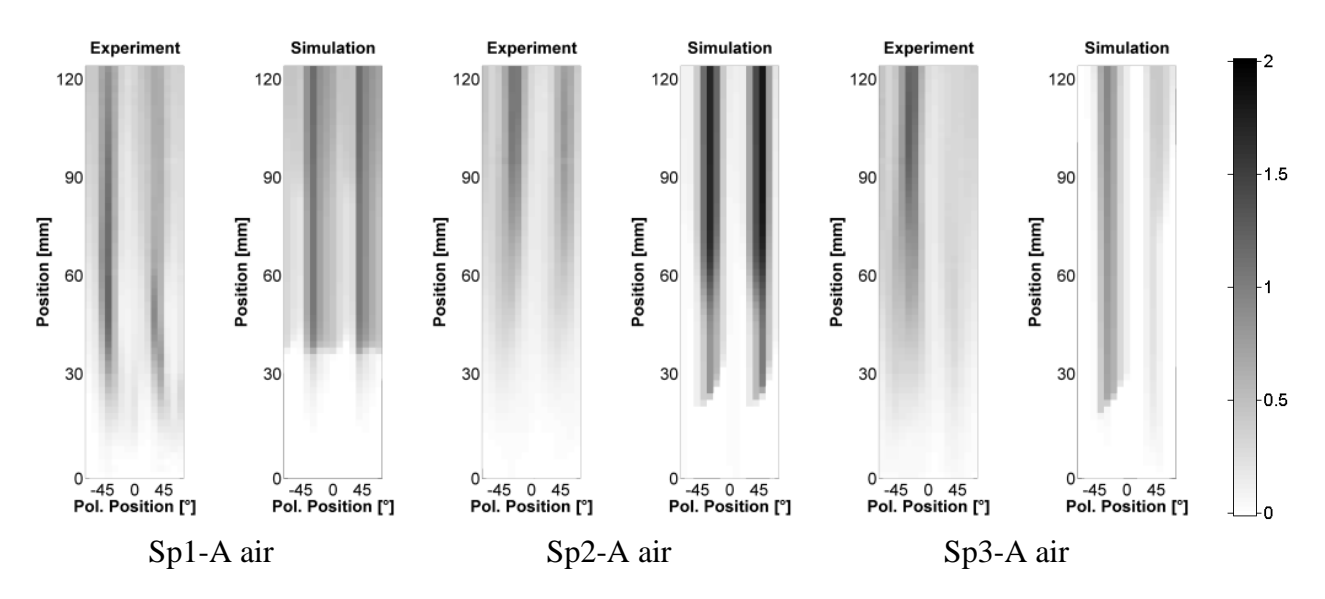


Figure 16 Comparison between experimental and modeled integral droplet deposition fraction distribution for different spacers and gases (J=30 m/s, exp. $1-\beta=0.002$)

4. Comparison with CFD Results

4.1 Model Validation against Experiments

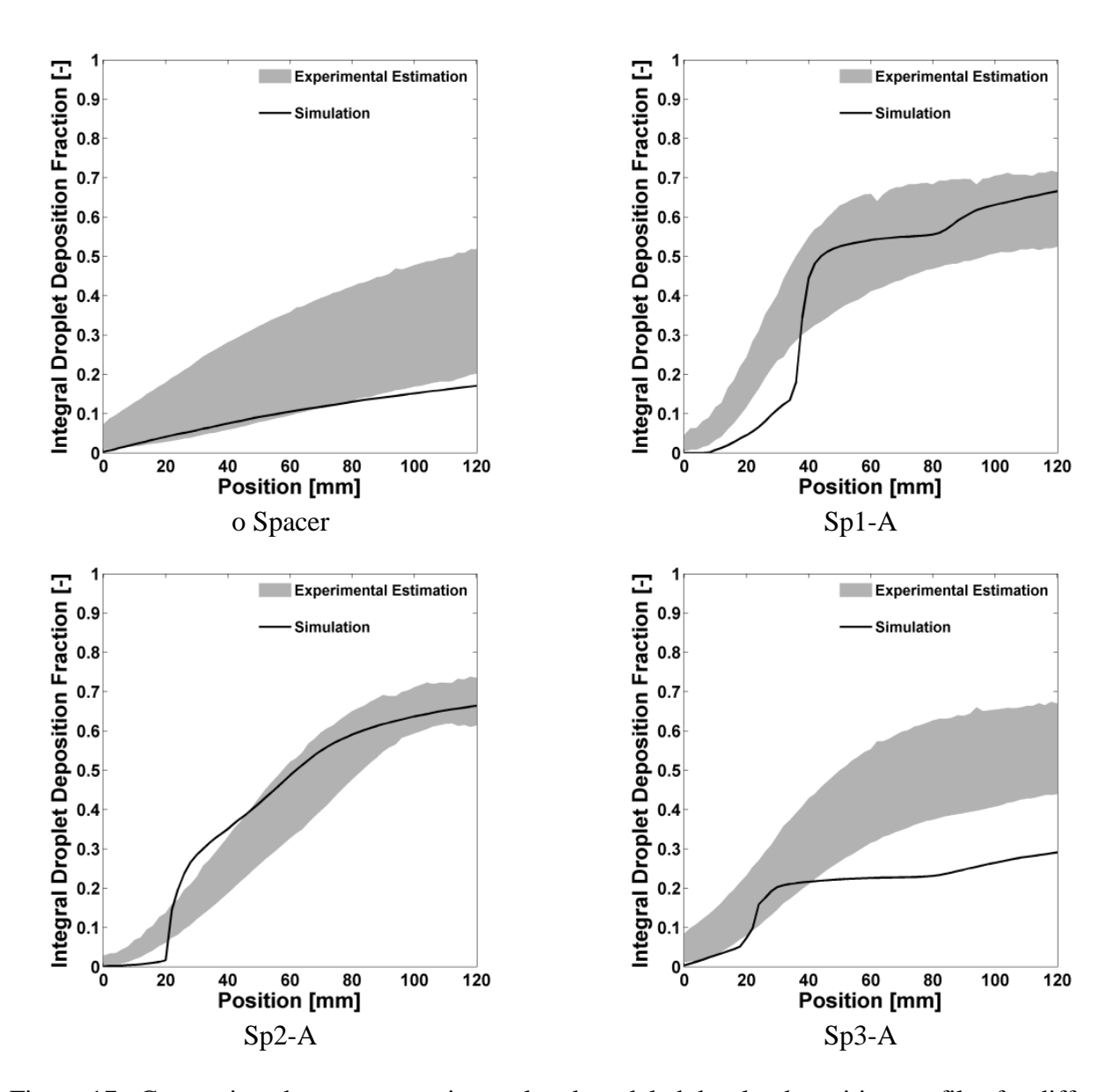


Figure 17 Comparison between experimental and modeled droplet deposition profiles for different spacers (air, J=20 m/s, $1-\beta=0.002 \text{ to } 1-\beta=0.010$)

Figure 16 shows the comparison between the experimental and modeled integral droplet deposition fraction, for three different spacers and air respectively C_4F_8 for a total flux of 30 m/s. Before it has been shown, that the experimental deposition rate is dependent of the flux ratio. To be closest to the condition of a dry wall, as assumed for the droplet experiment, the flux ratio is set to 0.002 for all displayed cases.

It should be noted, as discussed before, that the integral droplet mass flux determined experimentally is dependent on the liquid film advection and diffusion downstream of the spacer. This causes now some

distortion in the comparison, because the liquid film velocity field of the simulation results are assumed to point exclusively in axial direction.

In general experiments and simulation are in good qualitative agreement. The main deposition pattern, which is caused by the shading of the droplets by the spacer vanes, is captured well in the simulation results: The deposition in circumferential direction is predicted with quite high accuracy. On the other hand, the simulation is less diffuse than the experiments for the droplet deposition closest to the spacer. The reason is most probably found in the change of droplet size distribution in the spacer proximity due to droplet break-up, which causes a wider deposition spectrum.

Figure 17 shows the comparison between experimental and simulated integral deposition profiles for the spacers of the A-series and once without spacer. The grey area is the uncertainty in the estimation caused by the liquid film flow rate, which influences the deposition rate. Since in the simulations a dry wall is considered (the liquid film is not modeled), the experiments are strictly speaking not comparable with the simulations. It can be said though, that the best approximation is achieved by considering the lower edge of the area, as it represents the experiment with the thinnest liquid film. Compared to other gases and total fluxes, the chosen cases are the ones with the best agreement between simulations and experiments from a quantitative point of view. The comparison shows, that for all spacers the initial droplet deposition in the area of 20 mm to 50 mm downstream of the spacer is strongly overpredicted. The gradients seen in the experiments are weaker.

4.1.1 <u>Sensitivity Analysis</u>

The sensitivity analysis is conducted for one selected base case, which is an air-water flow with Sp2-A at a total flux of 30 m/s. The varied parameters or model features are listed below:

turbulent droplet dispersion (base case: dispersion on) turbulence model (base case: k-ε-model) mesh size (base case: 2 mm) advection scheme (base case: 2nd order) drop size distribution (base case: 0.4 mm) • injection cone angle (base case: 15°) initial droplet velocity (base case: 2.35 m/s) modeling of direct spacer impact (base case: droplet sliding)

It is found that the turbulent dispersion of the droplets has a negligible influence. This is not surprising considering that the τ_p^+ is far above 20 for all simulations. It should be kept in mind however, that droplet sizes can be significantly lower at the much higher pressure in a real BWR, which might result in a more pronounced influence of turbulent dispersion. The turbulent dispersion should therefore not be omitted from the model.

The sensitivity to the turbulence model, the mesh size and the advection scheme in the gas flow field calculation are summarized in

(top). Furthermore the results concerning the droplet deposition sensitivity to a variation of the boundary conditions describing the droplet injection are summarized in

(center), including injection cone, drop size distribution and initial velocity. Recall that these parameters are well known from the images of the high speed camera. Both parameter variations show that these parameters of the single phase gas RANS calculation as well as the injection parameters have only a small influence on the droplet deposition profile.

The highest sensitivity of the droplet deposition is found in the variation of the mechanism assumed for the modeling of direct impact of the droplets with the spacer (

bottom). This is unfortunately also the biggest unknown, since the interaction with the spacer most probably includes droplet breakup, film formation and change or loss of momentum of the liquid phase. Therefore some extreme assumptions were made for the sensitivity study:

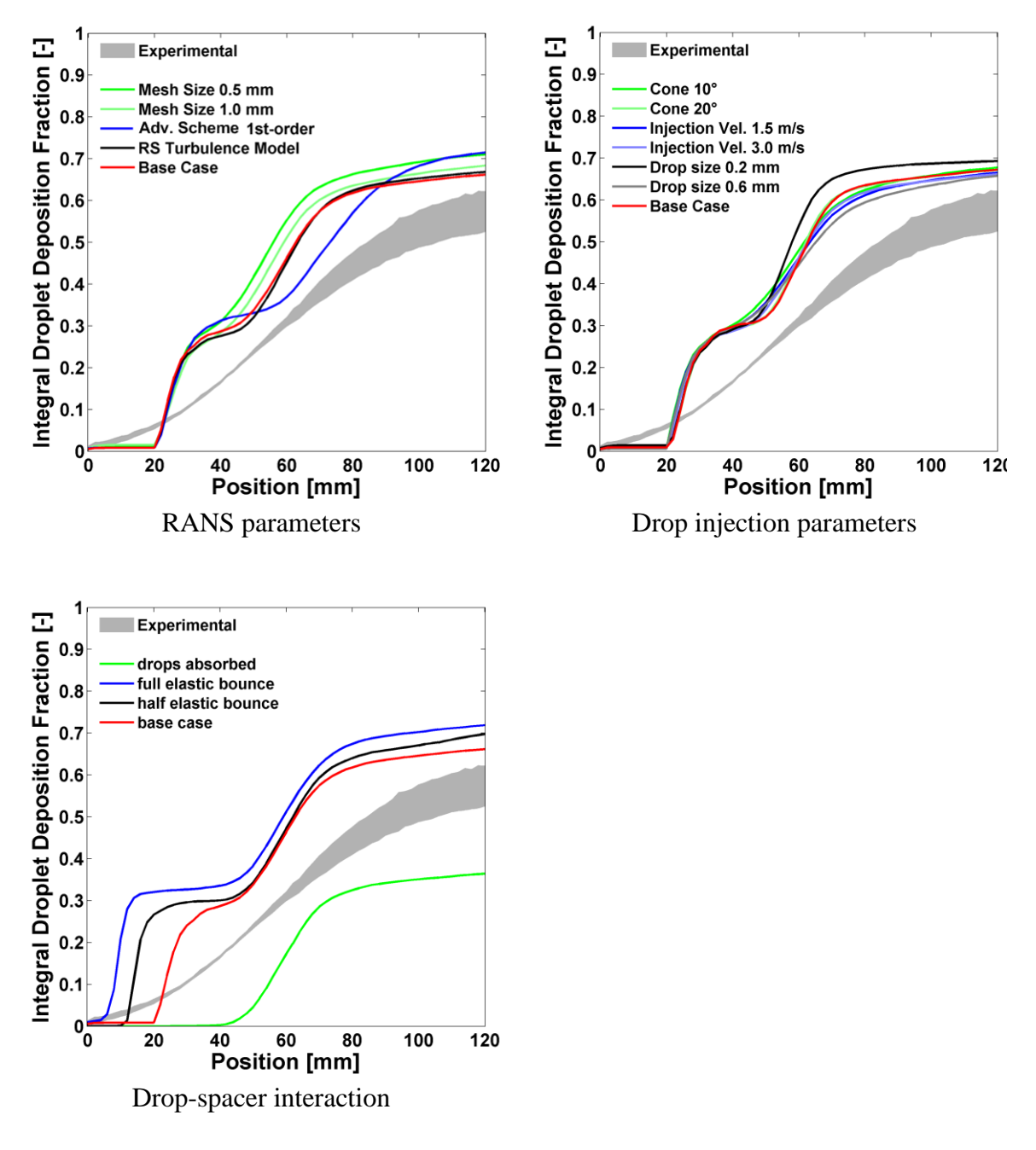


Figure 18 Sensitivity Analysis for chosen experiment (Sp2-A, air, J=30 m/s)

The large reduction in the deposition when assuming that droplets hitting the spacer are disappearing from the flow field (or in other words: modeled by an absorption of droplets hitting the spacer surface),

shows that the deposition between 20 and 40 mm downstream of the spacer is caused by the direct impact of droplets with the spacer.

For the case of an interaction, where secondary droplets leave the spacer after the impact, there are two bounding cases: The first assumes a fully elastic bounce, the second a total loss of momentum in the direction perpendicular to the spacer surface, which comes probably closest to a formation of a liquid film on the spacer surface. In both cases, the simplification is made that there is no breakup of the droplet. The Lagrangian transport of the droplet is not interrupted, only the velocity vector of the interacting droplet is changed according to the described kind of interaction during the impact. In case of loss of momentum perpendicular to the spacer surface, the droplet is moving parallel to this surface after the impact, which is basically equivalent to a sliding along the sensor surface. A case in between these extremes is a half elastic bounce, where the droplets lose half of the momentum in perpendicular direction. It is found that the closest reproduction of the experimental droplet deposition is achieved with the assumption of an elastic bounce of the droplets.

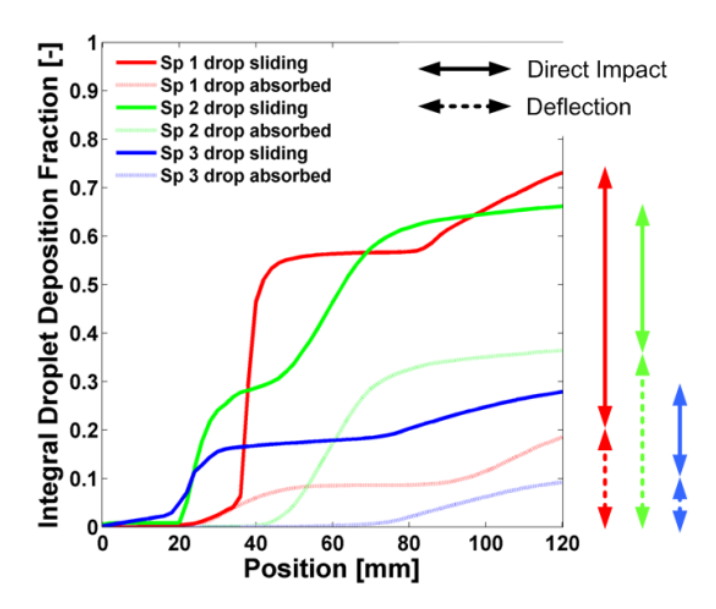


Figure 19 Simulated weighting of depositon effect for different spacers

(air, J=30 m/s)

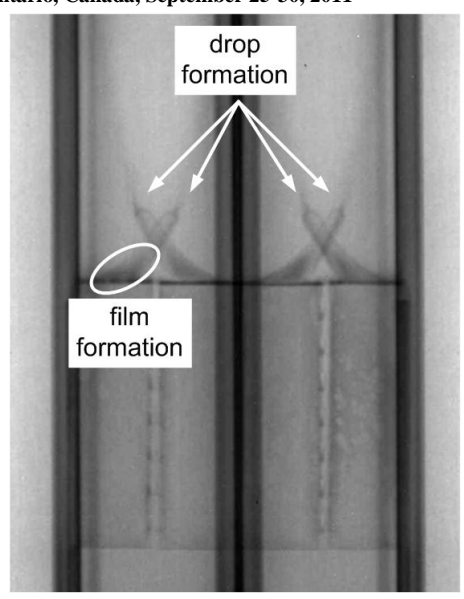


Figure 20 Image of the neutron tomography of Sp3-A for an air-water flow

Figure 19 shows that the weight between impact and deflection driven deposition enhancement is very distinct for different spacer geometries. This is done by switching on and off the impact driven deposition in the simulation. While for Sp1-A and Sp3-A the impact driven deposition plays the major role, the deflection and impact driven deposition are about equally responsible for the deposition enhancement of Sp2-A. It is important to be kept in mind that, as mentioned before, with smaller droplets in high density and temperature flows, the turbulent driven deposition may become more relevant. Finally the general conclusion can be drawn that the direct impact of droplets with the spacer seems to play a major role for the concentrated droplet deposition in close proximity of the spacer.

The model needs mainly to be improved in the

future by a more realistic simulation of the direct impact of droplets with the spacer. This includes a modeling of the liquid film build-up on the spacer, the droplet formation at rear edges of the spacer and the droplet break-up connected with the impact. An image of the neutron tomography in the same subchannel geometry [8] supports this insight: Figure 20 shows that at the tip of the vanes the liquid holdup is increased. Furthermore, a formation of a liquid film on the spacer is also visible. Another improvement is needed to enhance diffusivity for droplet deposition for both, impact and drag deflection driven deposition. This includes the modeling of droplet breakup in the spacer proximity due to higher gas shears, which most probably widens the droplet size spectrum. Moreover the increase of turbulence and shift towards lower turbulence frequencies by the presence of the liquid film could be responsible for this diffusivity. This means that the turbulence needs to be accounted for differently, than by a simple k-ɛ-model, including the formation of big eddies behind the spacer. Because of the major deficiencies of RANS turbulence models for complex flow geometries, this flow complexity can most probably only be solved by an Euler-Lagrangian LES approach, although this might lead to extreme computational efforts.

It is in general questionable, if RANS is the appropriate CFD method for subchannel flows with spacers, since RANS has severe difficulties to predict the turbulence in the presence of flow separations, as they are expected in the vicinity of the spacers. However it seems the only feasible approach for two reasons:

- The computational costs in the presence of the extremely high Reynolds numbers for a LES or DNS simulation is very high, even though they might predict flow separation better.
- Since the droplets of the experiments are mainly inertia controlled, the influence of a very
 accurate gas velocity field on the droplets is minor, seen in the sensitivity study for different
 turbulence models.

5. Conclusions

Droplet deposition and its enhancement by spacers is an important factor to delay dryout in BWRs. The major contribution of the deposition mechanisms is however mostly unknown, due to lack of highly resolved experimental data. The problem has been approached in the past by means of total mass

transfer measurements and amended simulations, which on the other hand could not be validated because of the lack of suitable data.

The experiments of this work are designed to offer validation to computational models, by providing high-resolution measuring data obtained under well-defined boundary conditions. The experiments are conducted with six different spacer types and three different gas densities. Droplet deposition is then evaluated with two different post-processing technique, yielding an estimate for mass deposition and amount of droplet impacts.

Complementing CFD simulations were performed, based on a single phase gas RANS simulation with an one-way coupled Lagrangian tracking for droplet tracking.

Following conclusions can be drawn from the experimental results:

- All spacer types enhance the droplet deposition compared to the experiments without spacer. The spacer shape, especially the blockage ratio, plays an important role in regard to deposition enhancement. The blockage ratio alone is however not enough to predict deposition.
- The droplet size distribution seems to shift towards smaller droplets by passing through the spacer, as especially for high gas densities less droplets are counted with the autoregressive filter compared to experiments without spacer.
- The direct impact of droplets on the spacer contributes most to the deposition enhancement, deflection plays an important but minor role. The contribution of each phenomena to the deposition enhancement is dependent on the spacer shape and flow condition. Turbulence enhancement is negligible concerning deposition in the experiments conducted.
- For better quantitative agreement between experiments and simulations, the CFD model needs to be extended in the future by modeling droplet breakup in spacer proximity and modeling the droplet impacts on the spacer accurately.

In regard to the spacer design and development it is important to keep in mind, that if the spacer is tested under BWR conditions, the main deposition effects might shift towards a deflection and even turbulent driven deposition, due to the smaller droplet size and higher gas shear. Since the two effects are of completely different physical nature, an optimized design in air-water experiments might actually not perform well in a BWR. Still the direct droplet-spacer impact is most probably one of the key factors of enhanced droplet deposition downstream of spacers, because the biggest mass transfer is achieved by big droplets with large relaxation times.

6. References

- 1. Damsohn, M. and H.M. Prasser, *High-speed liquid film sensor for two-phase flows with high spatial resolution based on electrical conductance*. Flow Measurement and Instrumentation, 2009. **20**(1): p. 1-14.
- 2. Damsohn, M. and H.M. Prasser, *High-speed liquid film sensor with high spatial resolution*. Measurement Science and Technology, 2009(11): p. 114001.
- 3. Damsohn, M. and H.M. Prasser, *Experimental studies of the effect of functional spacers to annular flow in subchannels of a BWR fuel element*. Nuclear Engineering and Design, 2010. **240**(10): p. 3126-3144.
- 4. D'Orio, *Patent No.: US* 5,790,624. United States Patent, 1998.
- 5. Nylund, Patent No.: US 6,816,563,B2. United States Patent, 2004.
- 6. Damsohn, M. and H.M. Prasser, *Droplet deposition measurement with high-speed camera and novel high-speed liquid film sensor with high spatial resolution.* NUTHOS-7: The 7th

- International Topical Meeting on Nuclear Reactor Thermal Hydraulics, Operation and Safety, Seoul, Korea, 2008.
- 7. Gosman and Ioannides, *Aspects of computer simulation of liquid-fueled combusters*. Journal of energy publ. of the American Institute of Aeronautics, 1983. **7**.
- 8. Kickhofel, J., R. Zboray, and H.-M. Prasser, *Cold neutron tomography of annular coolant flow in a double subchannel model of a boiling water reactor.* NIMA_PROCEEDINGS-D-10-00785, South Africa, 2010.